AD_____

Award Number: W81XWH-08-1-0365

TITLE: Onboard SPECT for Localizing Functional and Molecular Targets in Metastatic Breast Cancer

PRINCIPAL INVESTIGATOR: Justin R. Roper, B.S.

CONTRACTING ORGANIZATION:
Duke University
Durham, NC 27710

REPORT DATE:
July 2009

TYPE OF REPORT:
Annual Summary

PREPARED FOR: U.S. Army Medical Research and Materiel Command
Fort Detrick, Maryland 21702-5012

REPORT DOCUMENTATION PAGE

Form Approved
OMB No. 0704-0188

1. REPORT DATE *(DD-MM-YYYY)*	**2. REPORT TYPE**	**3. DATE COVERED** *(From - To)*
01-07-2009	Annual	01July2008 - 30Jun2009

4. TITLE AND SUBTITLE
Onboard SPECT for Localizing Functional and Molecular Targets in Metastatic Breast Cancer

5a. CONTRACT NUMBER

5b. GRANT NUMBER
W81XWH-08-1-0365

5c. PROGRAM ELEMENT NUMBER

6. AUTHOR(S)
Justin R. Roper

5d. PROJECT NUMBER

5e. TASK NUMBER

5f. WORK UNIT NUMBER

7. PERFORMING ORGANIZATION NAME(S) AND ADDRESS(ES)

Duke University
Durham, NC 27710

8. PERFORMING ORGANIZATION REPORT NUMBER

9. SPONSORING / MONITORING AGENCY NAME(S) AND ADDRESS(ES)
U.S. Army Medical Research and Materiel Command
Fort Detrick, Maryland 21702-5012

10. SPONSOR/MONITOR'S ACRONYM(S)

11. SPONSOR/MONITOR'S REPORT NUMBER(S)

12. DISTRIBUTION / AVAILABILITY STATEMENT
Approved for public release; distribution unlimited

13. SUPPLEMENTARY NOTES

14. ABSTRACT

The overall goal of this work is to assess the feasibility of using single photon emission computed tomography (SPECT) for imaging inside radiation therapy treatment rooms to localize functional & molecular targets associated with metastatic breast cancer. A computer simulation was performed using a female NCAT phantom that had various tumor diameters and uptake ratios located in bone, chest wall and lung. SPECT scans were simulated for an anterior half-circular orbit that avoided the flat-top treatment couch. Image ensembles were generated for scan times of 4, 8 and 10 minutes. Localization of tumor centroids was assessed using nonprewhitening numerical observers. Localization was strongly dependent on tumor location relative to the detector trajectory, thus suggesting the need for custom detector trajectories. Certain results were encouraging. Localization accuracy was within 2 mm for 1.44- and 2.16-cm anterior tumors with 6:1 uptake ratios using 4 minute scans. Future work includes hardware studies to validate these results.

15. SUBJECT TERMS
SPECT, Radiation Therapy, Onboard Imaging, Target Localization

16. SECURITY CLASSIFICATION OF:			**17. LIMITATION OF ABSTRACT**	**18. NUMBER OF PAGES**	**19a. NAME OF RESPONSIBLE PERSON**
					USAMRMC
a. REPORT	**b. ABSTRACT**	**c. THIS PAGE**	UU	20	**19b. TELEPHONE NUMBER** *(include area code)*
U	U	U			

Table of Contents

Introduction

The overall goal of this work is to assess the feasibility of using single photon emission computed tomography (SPECT) for imaging inside radiation therapy treatment rooms to localize functional & molecular targets associated with metastatic breast cancer. The first aim is to evaluate localization accuracy and precision as a function of scan time, tumor size, tumor-to-background uptake ratio, and background non-uniformity. A computer simulation was performed using a female NCAT phantom that had spherical tumors (functional targets) of various diameters and uptake ratios located in bone, chest wall and lung [1]. SPECT scans were simulated for an anterior half-circular orbit that avoided the flat-top treatment couch and the supine phantom. Ensembles of independent, noisy projection images were generated for different scan times. Localization of tumor centroids was assessed using nonprewhitening numerical observers for a MAFC task. Localization accuracy was strongly dependent on tumor location relative to the detector trajectory, with better results in the anterior portions of the phantom near the chest wall where attenuation was less severe and spatial resolution better as compared with regions near the spine. These results suggest the need for custom detector trajectories specific to tumor sites instead of a general purpose detector trajectory. Also important to localization was the tumor-to-background activity ratio. Longer scan times were needed for comparable localization of lower-contrast lesions, and as such has important implications for the selection of potential radiotracers since short imaging times are needed to minimize patient motion and to maintain therapy-machine throughput. Certain results were encouraging from the simulation study: Localization accuracy was within 2 mm for 14.4- and 21.6-mm anterior tumors with 6:1 uptake ratios using 4 minute scans, suggesting that on-board SPECT may be useful for localizing certain functional & molecular targets. Future work includes hardware studies to validate these results.

Body

Specific Aim 1: Evaluate localization accuracy and precision as a function of scan time, tumor size, tumor-to-background uptake ratio, and background non-uniformity.

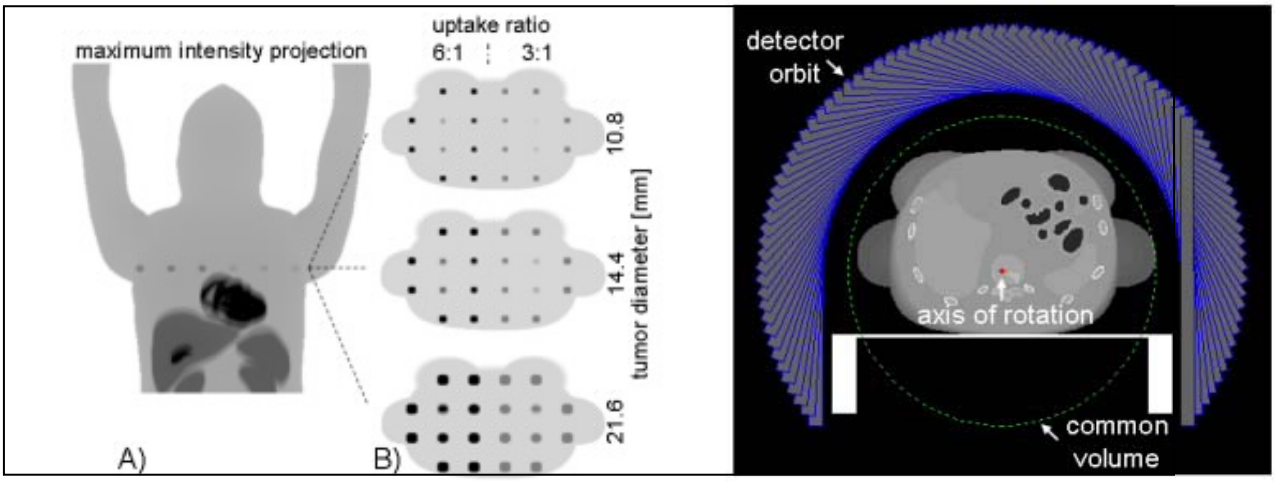

Fig.1. Activity distribution (LEFT) simulating ^{99m}Tc-sestamibi with tumors located in a transaxial slice superior to the heart. Three tumor diameters and two uptake ratios were investigated. (RIGHT) Attenuation map for 140 keV photons from ^{99m}Tc shown with anterior half-circular detector orbit. [1]

Tumors were simulated with various diameters – 10.8, 14.4 and 21.6 mm – and with uptake ratios of 3:1 and 6:1 relative to background and were located in bone, lung and soft tissue of a female NCAT phantom (Fig. 1). The 8 deepest tumors were positioned in lung and were subject to the effects of respiratory motion. The same motion vectors were applied to laterally-symmetric lung tumors in order to minimize differences other than activity uptake ratios. Background activity was non-uniform for tumors near the heart. An anterior, half-circular detector trajectory was used to avoid viewing through the flat-top treatment couch. The simulated projection images included the effects of distance-dependent spatial resolution and non-uniform attenuation. Scatter was not considered. Projections were degraded with Poisson Noise to form ensembles of 25 independent noisy realizations for scans times of 4, 8 and 20 minutes. Images were reconstructed with attenuation correction using 6-subset, 5-iteration OSEM. Representative reconstructed images are shown in Fig. 2 from the image ensembles.

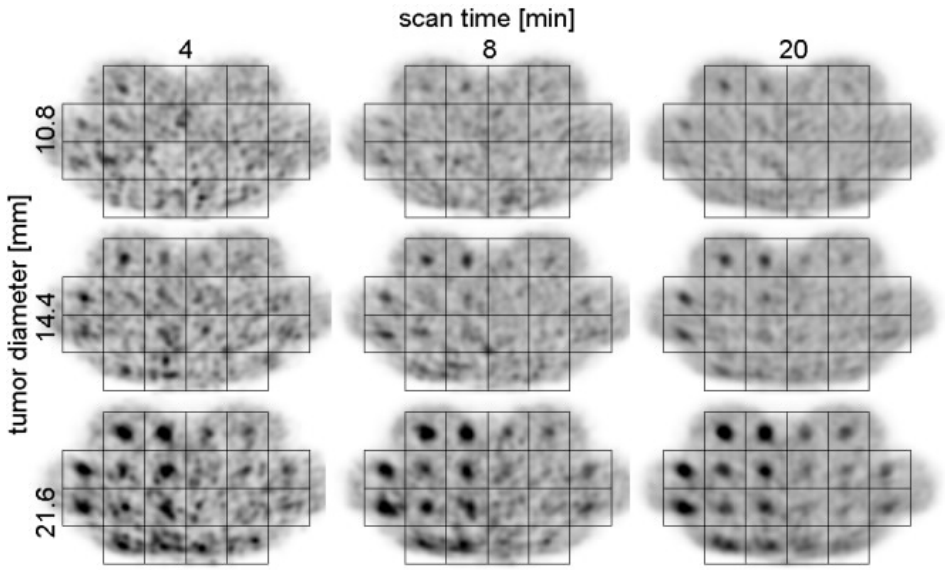

Fig. 2. Sample reconstructed images for each tumor diameter and scan time. Grids are superimposed on images such that true tumor locations are centered within the grid squares. [1]

Tumor centroids were localized using nonprewhitening numerical observers (NPW filters) for a multiple alternative forced choice (MAFC) task where one and only one tumor was located within each 28.8-mm-diameter search volume. NPW filters were generated by blurring true tumor geometries with a 14.4-mm-FWHM Gaussian kernel, which approximates image spatial resolution. A NPW filter was slid throughout each search volume and the location with the highest cross correlation was selected as the measured tumor centroid. Euclidean distances between the measured and true centroid locations were computed over the image ensembles yielding estimates of mean error -- localization accuracy -- and standard deviation of error – localization precision. Estimates of localization accuracy and precision are reported in Fig. 3 for the investigated tumor diameters, anatomical locations, tumor-to-background activity ratios and scan times.

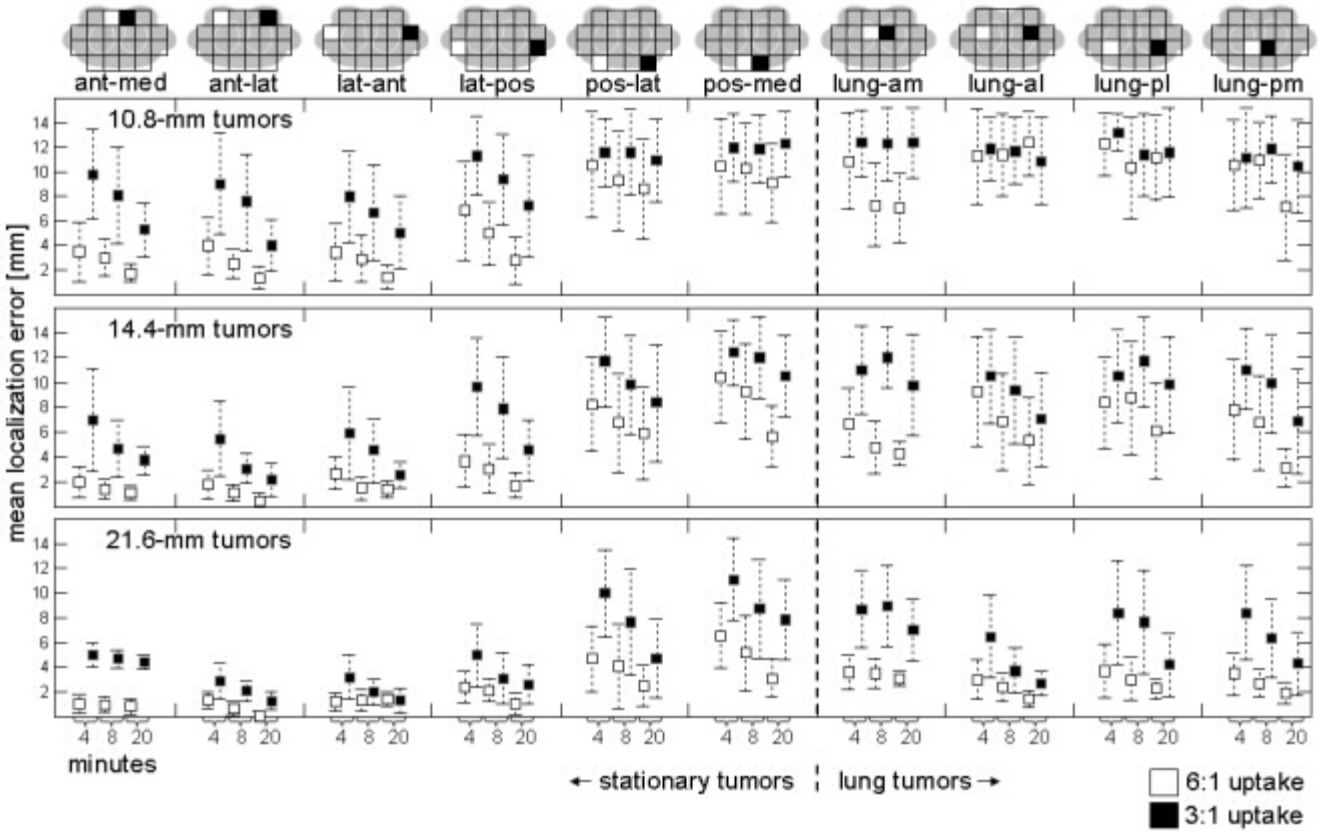

Fig. 3. Localization accuracy – boxes – and localization precision – error bars – displayed as a function of tumor size, anatomical location, tumor-to-background activity uptake ratio and scan time. [1]

The results in Fig. 3 have important implications for using on-board SPECT to localize metastatic breast cancer. For stationary tumors of the same diameter and uptake ratio, localization accuracy varied substantially depending on tumor location relative to the detector trajectory. Localization accuracy was vastly better in the chest wall than near spine. These differences are due to the effects of attenuation and distance-dependent spatial resolution. Because of the anterior detector trajectory, relatively fewer counts from tumors near the spine escaped the phantom, and those that did escape were blurred over a larger number of detector bins as compared with counts from tumors near the chest wall. While the investigated half-circular detector trajectory yields highly variable localization values and does not appear to be a one-size-fits-all acquisition strategy, it is important to note that the task of on-board SPECT likely would not be to image a large volume, e.g., the upper torso. Instead the task would be to image a relatively small region near tumor. Since tumor location is known approximately from treatment planning images, detector trajectories could be customized for certain anatomical locations to mitigate the effects of attenuation and distance-dependent spatial resolution. Further research is needed to determine impact of custom detector trajectories on target localization, given the constraints of the treatment couch, particularly for posterior tumors where localization was generally poor using an anterior detector trajectory.

Results from Fig. 3 also demonstrate the importance of radiotracer specificity. Tumors in laterally-symmetric anatomical locations differed primarily by tumor-to-background activity ratios. For those tumors where SPECT was useful for localization, tumors of 6:1 uptake were typically localized as well using 4-minute scans as tumors of 3:1 uptake using 20-minute scans. Because short imaging times are necessary to minimize patient motion and for machine throughput, radiotracers with a high differential uptake between tumor and nearby healthy tissue would be most appropriate for on-board SPECT imaging. Additionally, treatment planning images could be used to estimate tumor-to-background activity ratios to determine which patients might benefit from on-board SPECT guided radiation therapy. Planning images can also be used to estimate tumor size, another important criterion for patient selection since localization accuracy is strongly related to tumor diameter, as shown in Fig 3.

Non-uniform background activity from the heart proved challenging for localizing tumors of 3:1 uptake in the medial chest wall. These tumors are denoted by black boxes in the first column of Fig 3. For the 21.6-mm-diameter tumors, error bars are much smaller than the total error, demonstrating a bias that can be visualized in reconstructed images. Apparent tumor activity is suppressed inferiorly near the heart and causes the measured tumor centroid to shift superiorly. Additional research is needed to improve target localization near hot background objects.

Localization was generally poor in the lungs, and further work is needed to investigate the impact of respiratory gating on localization. As expected, localization accuracy and precision usually improved with increasing scan time. For the shortest scan time, certain results from this simulation study were encouraging. Localization accuracy was within 2 mm for anterior tumors of 6:1 uptake that were14.4 mm or larger in diameter using 4-minute scans. This scan duration is likely compatible with limited-fraction, high-dose-per-fraction therapies like stereotactic body radiation therapy were additional time is allowed for patient positioning.

Further details pertaining to this study may be found in [1], which is located in Appendix D.

Hardware studies are currently underway to understand the effects of scatter on target localization.

Key Research Accomplishments

Year 1:

A computer simulation study was performed to address Aim 1: Evaluate localization accuracy and precision as a function of scan time, tumor size, tumor-to-background uptake ratio, and background non-uniformity. (Please see Appendix A.) This work was published in a peer-reviewed journal – Medical Physics. (Please see article in Appendix D.) A follow-up hardware study is currently underway that will complete Aim 1.

My research has been presented at conferences hosted by AAPM and ASTRO. Published abstracts are provided in Appendices B-C.

Other Tasks Related to BCRP Predoctoral Traineeship:
(Appendix A)

• I have gained a better understanding of clinical care for breast cancer patients through interactions with physicians from radiology and radiation oncology at Duke University. More specifically, I have attended the Joint Breast Conference where patient charts are reviewed by surgeons, oncologists, radiation oncologists, pathologists, nurses,

and others involved in patient care to determine the best course of treatment. Further, I have completed the Nuclear Medicine Practicum offered by the Medical Physics Graduate Program where I spent time in a reading room with radiologists who explained the strategies and challenges of interpreting nuclear medicine images.

• I have participated in and presented my research at journal clubs and seminars hosted by the Medical Physics Graduate Program and by the Department of Radiation Oncology. During the past year, I was responsible for organizing weekly research meetings in the Physics Division of Radiation Oncology where ongoing research was presented by graduate students and postdoctoral researchers.

• I have completed the minimum number of courses required by the Medical Physics Graduate Program and fulfilled all teaching assistantships. During the spring semester, I participated in an independent study involving IMRT treatment planning under the supervision of a senior medical physicist. Through this course, I gained practical skills for creating treatment plans that deliver prescribed dose to tumor while sparing healthy tissues.

• Results from this report were included in my preliminary exam proposal and presentation, “On-board SPECT Imaging for Localizing Biological Targets”, which was accepted by my committee on April, 20 2009.

Reportable Outcomes

Peer-reviewed article

JR Roper, JE Bowsher, FF Yin. “On-board SPECT for localizing functional targets: A simulation study.” Med. Phys. Volume 36, Issue 5, pp. 1727-1735 (May 2009)

Presentations and published abstracts

JR Roper, JE Bowsher, FF Yin. “Quantitative Analysis of On-board SPECT Imaging Using Compact Gamma Cameras.” Poster presentation at the *50th Annual AAPM Annual Meeting*, Houston, TX, 27 – 31 Jul. 2008.

JR Roper, AA Manzoor, JB Bowsher, FF Yin, S-M Zhou, TZ Wong, S Borges-Neto, JL Hubbs, S Demirci, LB Marks. “Are post-RT cardiac perfusion defects due to cardiac toxicity, or are they artifacts from attenuation changes in surrounding soft tissues?” Poster presentation at the *50th Annual ASTRO Meeting*, Boston, MA, 21 – 25 Sept. 2008.

Conclusion

On-board SPECT was investigated for localizing functional & molecular targets associated with metastatic breast cancer. A computer simulation study was performed to characterize localization accuracy and precision as a function of scan time, tumor size, tumor-to-background uptake ratio, and background non-uniformity. Results show the importance of the detector trajectory and suggest need for custom detector trajectories for imaging different tumor sites. As expected localization accuracy and precision improved with increasing tumor size and scan time. Using relatively short 4-minute scans, localization accuracy was within 2 mm for certain tumors. These encouraging results warrant further research.

References

[1] JR Roper, JE Bowsher, FF Yin. “On-board SPECT for localizing functional targets: A simulation study.” Med. Phys. Volume 36, Issue 5, pp. 1727-1735 (May 2009)

Appendix A

Specific Aim 1: Evaluate localization accuracy and precision as a function of scan time, tumor size, tumor-to-background uptake ratio, and background non-uniformity.

A. Hardware Phantom Studies (Months 1- 8)
- a. Fillable hot spheres in a lower-activity cylindrical background, approximately mimicking the geometry of supraclavicular lymph nodes
- b. Sphere diameters ranging from 8mm to 24mm
- c. Lesion-to-background uptake ratios of 2:1, 5:1, and 10:1
- d. Background non-uniformity: 40mm sphere with an offset inner 8mm sphere
- e. Activity ratios of 10:2:1 and 10:5:1 in the outer sphere, inner sphere, and background
- f. Acquire projection images using a Trionix Triad XLT SPECT scanner.
- g. Scan times from 1 minute to 24 minutes
- h. Acquire CT image of the same phantom (See 1B below).
- i. From ensemble of images, evaluate the following as a function of scan time, tumor size, tumor-to-background uptake ratio, and background non-uniformity:
  - i. Evaluate contrast-to-noise ratios (CNRs)
  - ii. Evaluate MAFC
- j. Prepare and submit paper on this work. (Months 7- 8)

B. Use Above Hardware Data to Validate Computer-Simulation Studies (Months 9-12)
- a. Generate software phantom by digitizing the CT image of the 1A hardware phantom.
- b. Repeat 1A studies using the digital, software phantom.
- c. Compare hardware and software studies, in order to validate the software approach (which is employed below in 2A-3A).

Specific Aim 2: Evaluate the effect of respiratory motion on the accuracy and precision of target localization.

A. Software Studies using Digital Anthropomorphic Phantom (Months 13-19)
- a. Hot spherical lesions surrounded by warm background activity in torso of NCAT anthropomorphic phantom, simulating breast cancer metastasis in bone, lung, and lymph nodes.
- b. Lesion sizes ranging from 8mm to 24mm
- c. Radiotracer uptake ratios of 2:1, 5:1, and 10:1 in lesions and background
- d. Scan times ranging from 1 minute up to 24 minutes
- e. Generate ensembles of breath-hold images
- f. Evaluate CNR and MAFC as function of lesion size, lesion-to-background uptake ratio, and scan time.

B. Digital Anthropomorphic Phantom with Respiratory Motion (Months 20- 28)
- a. Enable respiratory motion features within NCAT software.
  - i. Model ungated onboard SPECT imaging during free breathing
  - ii. Model gated onboard SPECT imaging during free breathing
- b. Repeat 2A studies with the addition of respiratory motion
- c. Calculate CNR and MAFC as a function of lesion size, lesion-to-background uptake ratio, scan time, and scan mode (as described in 2Bai-ii)
- d. Prepare and submit paper for work in 2A-B. (Months 27- 28)

Specific Aim 3: Evaluate the impact of limited detector surface area, and consequent projection-data truncation, on the accuracy and precision of target localization.

A. Software Studies using Truncated Detector Field of View (FOV) (Months 29-36)
- a. Truncate projection images from 2A to simulate detectors with smaller surface areas.
- b. Detector FOV ranging from 15x15cm2 to 20x40cm2
- c. Investigate the dependence of CNR and MAFC on detector FOV.
- d. Evaluate the relationship between detector FOV and truncation artifacts.
- e. Write and submit paper (Months 35-36)

Other Tasks Related to BCRP Predoctoral Traineeship.

A. Shadow radiologist(s) to better understand breast cancer diagnoses and staging. (Months 1-12)
B. Shadow radiation oncologist(s) to learn about breast cancer therapies. (Months 1-12)
C. Participate in weekly journal clubs and seminars. (Months 1-36)
D. Audit courses relevant to my breast cancer research project (Months 1-36)
E. Present research at conferences such as AAPM, ASTRO, and the Era of Hope Meeting. (Months 1-36)
F. Gain experience with RT medical physics (e.g. treatment planning & quality assurance). (Months 12-36)
G. Prepare and defend PhD dissertation (Months 30-36)

Appendix B

Quantitative Analysis of a Compact On-board SPECT Detector for ROI Reconstruction

JR Roper, JE Bowsher, FF Yin

Purpose: Single photon emission computed tomography (SPECT) imaging on-board radiation therapy machines may enhance radiation therapy. Use of a light-weight, compact detector would be desirable because of maneuverability, yet is challenged by truncation and consequently reconstruction artifacts. We hypothesize that, for a sizeable volume surrounding the tumor target, and with properly chosen detector trajectories, compact detectors can provide image quality that is comparable to that of full-size SPECT detectors.

Methods and Materials: On-board SPECT imaging was computer simulated for detectors with active surface widths of 21.2 and 40.0 cm. Detector trajectories were selected such that the common volume encompassed an 8-cm-diameter ROI surrounding each tumor in the torso of a NCAT phantom. For deep tumors, two common volumes – interior and partially exterior – were investigated. Radiotracer distribution was modeled for 99mTc-Sestamibi. Noise-free and noisy projection images were generated with an analytical simulator that models non-uniform attenuation, collimator & detector efficiency, and spatially-varying spatial resolution. Images were reconstructed by OSEM. In reconstructed images, root mean square error and recovered tumor activity were analyzed as a function of detector width and detector trajectory.

Results: Image truncation reduced overall image quality. For example, RMS error over an entire noise-free image slice was 18 – 35% worse with the 21-cm-wide detector versus the larger detector. However, for regions within the common volume for both detector widths, RMS errors differed by less that 2%. Similar results were observed for noisy images. Moreover, the recovered fraction of tumor activity was comparable, except for when the smaller-detector common volume was interior – the recovered activity was reduced by 11%.

Conclusions: Preliminary results show that an 8-cm-diameter ROI can be reconstructed using 21 or 40-cm-wide detectors with comparable RMS errors and recovered tumor activities, supporting the proposal that on-board target localization could be accomplished using compact SPECT detectors.

Appendix C

Are post-RT cardiac perfusion defects due to cardiac toxicity, or are they artifacts from attenuation changes in surrounding soft tissues?

JR Roper, AA Manzoor, JB Bowsher, FF Yin, S-M Zhou, TZ Wong, S Borges-Neto, JL Hubbs, S Demirci, LB Marks.

Purpose: Following RT for left-sided breast cancer, perfusion defects (i.e. cold regions) are often noted on SPECT images. Almost all new defects are in the cardiac apex. Since SPECT is not absolutely quantitative, defects are detected by comparing regional intensities on pre-RT and post-RT images. Further, as SPECT images are not corrected for attenuation, and since RT may increase soft tissue density, apparent defects may be, at least partially, attributable to changes in attenuation of surrounding soft tissue. We herein perform a series of computer-based simulations to assess this possibility.

Methods: The perfusion tracer ^{99m}Tc-Sestamibi was simulated in a female NCAT phantom. Two tangential breast fields were considered: the deep border of one excluded the heart while a second included 2.5 cm of anterior heart. Within RT fields, tissue densities were increased in increments of 10% up to 50%. Noise-free images were simulated for a cardiac SPECT protocol – 180^{o} circular orbit, 60 views, parallel hole collimation – by modeling photon detection efficiency, distance-dependent spatial resolution, and non-uniform attenuation. Images were reconstructed without attenuation correction by OSEM (10 subsets, 20 iterations) onto a grid with 0.36 cm wide voxels. For varying degrees of change in soft tissue density, apparent reductions within the apex were noted, and compared with effects elsewhere. Simulations were repeated with the left (222 ml) breast removed to model mastectomy.

Results: As tissue density is increased by 10, 20, 30, 40, and 50%, corresponding reductions in apparent apical perfusion, for the different scenarios, are, respectively:

intact breast, 2.5 cm heart in field	13, 24, 34, 42, 50%;
intact breast, heart sparing	8, 15, 22, 28, 34%;
mastectomy, 2.5 cm heart in field	10, 19, 26, 34, 40%;
mastectomy, heart sparing	5, 9, 14, 18, 21%.

Changes in cardiac perfusion were not uniform; the apex was affected more than other areas.

Conclusion: RT-induced increases in soft-tissue attenuation can cause apparent changes in apical perfusion that might account for some of the defects seen clinically. However, the simulations also suggest that apparent defects should be seen even if the heart is excluded from the RT beam. Since perfusion defects are rarely seen in patients with no heart in the field, the possible changes in soft tissue attenuation/density are likely not the primary cause of perfusion defects seen clinically. Additional work is needed to understand the degree and impact of RT-induced soft tissue changes.

Appendix D

JR Roper, JE Bowsher, FF Yin. “On-board SPECT for localizing functional targets: A simulation study.” Med. Phys. Volume 36, Issue 5, pp. 1727-1735 (May 2009)

On-board SPECT for localizing functional targets: A simulation study

Justin Roper,[a] James Bowsher, and Fang-Fang Yin
Department of Radiation Oncology, Medical Physics Graduate Program, Duke University Medical Center, Durham, North Carolina 27710

(Received 29 September 2008; revised 23 February 2009; accepted for publication 16 March 2009; published 16 April 2009)

Single photon emission computed tomography (SPECT) was investigated for imaging on-board radiation therapy machines in order to localize functional and molecular targets. A computer-simulated female NCAT phantom was positioned supine on a flat-top treatment couch. Twenty tumor locations were defined in the upper torso. The eight lung tumors were subject to the effects of respiratory motion. Tumor diameters of 10.8, 14.4, and 21.6 mm were simulated for tumor-to-background ratios of 3:1 and 6:1 that are characteristic of the radiotracer ^{99m}Tc-sestamibi. Projection images representing scan times of 4, 8, and 20 min were simulated for an anterior, half-circular trajectory. Images were reconstructed with attenuation correction by ordered-subsets expectation maximization (OSEM) using six subsets and five iterations. Contrast-to-noise ratios (CNRs) were calculated from ensembles of 25 images. Cross correlation with a noise-free tumor template was used to select the most suspicious tumor location within a 14.4-mm-radius search volume surrounding each tumor, with only that one tumor in each search volume. Localization accuracy was assessed by calculating average distances between measured and true tumor locations. Localization accuracy and CNRs were strongly affected by tumor location relative to the detector trajectory. For example, CNR values near the chest wall were greater by a factor of 3.5 than for tumors near the spine and posterior ribs, a much greater effect than the factor of 1.6 difference in CNR between 6:1 and 3:1 tumor uptakes. Typically, tumors of 6:1 uptake were localized as accurately with 4 min of scan time as tumors of 3:1 uptake that had been imaged for 20 min. Using 4 min scans, 14.4 and 21.6 mm anterior tumors of 6:1 uptake were localized within 2 mm. These results suggest that SPECT, on-board radiation therapy machines, may be a viable modality for localizing certain functional and molecular targets using relatively short scan times. [DOI: 10.1118/1.3113902]

Key words: SPECT, on-board imaging, target localization

I. INTRODUCTION

Functional imaging modalities such as positron emission tomography (PET) and single photon emission computed tomography (SPECT) rely on radiotracers to identify physiological processes—such as angiogenesis, apoptosis, hormone receptor status, hypoxia, and proliferation—that have important implications in cancer management.[1] In the context of radiation therapy, such functional information can be used to define biological target volumes and, when combined with the dose sculpting capabilities of intensity modulated radiation therapy (IMRT), may provide enhanced therapeutic success.[2] To date, SPECT and PET have been utilized for diagnosis, staging, and treatment planning. We propose that functional imaging may also have an important role in the treatment room for the delivery of radiation therapy. Currently, treatment-room imaging is composed mainly of x-ray transmission imaging and ultrasound imaging, which are predominantly anatomical imaging modalities.[3] Imaging with these modalities immediately prior to delivery has improved patient alignment and reduced normal tissue damage for some sites,[3] but there are limitations. Notably, anatomical differences between tumor and surrounding tissue may not be substantial enough to directly visualize tumor. Consequently, localization is often performed instead with indirect markers such as bony anatomy, that may not necessarily indicate tumor position.[4–6] This limitation may be particularly important when high gradients are used to sculpt dose around biological targets that cannot be visualized using current treatment-room imaging modalities. Further, ultimately radiation therapy may be directed to temporally varying functional targets, such as hypoxia, which at treatment time may be in a location different from their location during planning CT or planning functional imaging.[7]

One possible method for directly localizing biological targets is to image with SPECT inside radiation therapy treatment rooms. SPECT has been used for a wide array of tumor imaging applications,[8,9] and ongoing research is expanding the already broad array of radiotracers.[10–15] While spatial resolution is somewhat limited compared with many anatomical imaging modalities, contrast between tumor and background can be substantially greater, and this stronger tumor signal may improve treatment-room tumor localization.

Though SPECT has been studied extensively for diagnostic tasks, SPECT has not been developed for the treatment-room environment where new challenges await. Notably, SPECT scans typically last 20 min or more, and this amount of time is too long in terms of patient motion and machine throughput. Shorter imaging times are needed, which implies

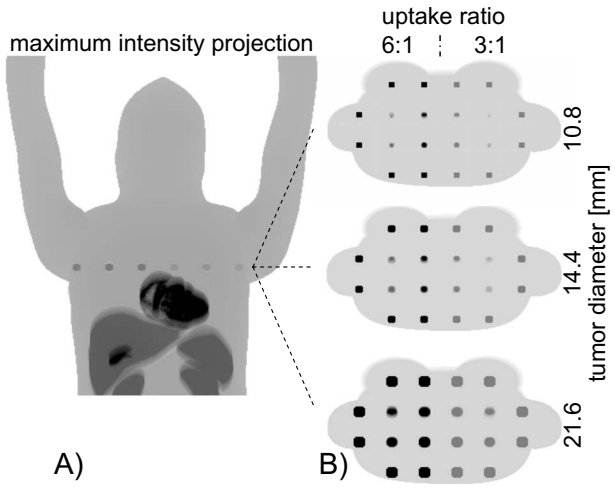

FIG. 1. (A) Coronal view of radiotracer distribution in phantom; (B) uptake pattern for different tumor sizes in transaxial slice.

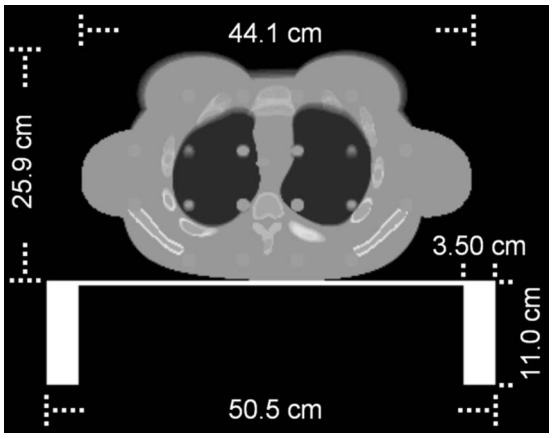

FIG. 2. Attenuation map of phantom and treatment couch with dimensions.

greater image noise. Additionally, treatment-room couches are wider and supporting rails are typically deeper than diagnostic SPECT couches. As such, treatment couches may challenge detector-to-patient proximity and increase attenuation, which in turn degrade image quality with poorer spatial resolution and increased noise. While these constraints will negatively impact image quality, it is important to consider that the task for on-board SPECT would be different than with most diagnostic SPECT scans. Because target size and approximate location are known, it may be possible to accurately localize functional targets. Furthermore, SPECT detector trajectories can be optimized for imaging the treatment region, a factor which may enhance SPECT images in the region of interest (ROI) as compared to diagnostic scans which typically have to survey a larger volume.

II. METHODS AND MATERIALS

II.A. Phantom

A female anthropomorphic phantom was generated with NCAT software.[16,17] The phantom was placed supine on a flat-surface treatment couch. Twenty tumor locations were arranged periodically on a square grid with centroid-to-centroid spacing of approximately 6 cm. Tumors were centered on voxels in an axial slice superior to the heart. For each tumor location, three tumor diameters—10.8, 14.4, and 21.6 mm with true volumes of 0.980, 2.10, and 6.49 cm^3—were simulated in separate phantoms as shown in Fig. 1. The 8 deepest tumors were located in the lungs where they were subject to respiratory motion, while the remaining 12 tumors were stationary in soft tissues or bone. Activity distribution was modeled for the radiotracer ^{99m}Tc-sestamibi that has been used to image a number of tumors, including breast cancer and its metastases.[18–20] Activity concentrations were 5.0 μCi/ml in the gall bladder and myocardium, 2.5 μCi/ml in the liver, kidneys, and spleen, and 0.25 μCi/ml in other healthy tissues. Left- and right-sided tumor activity concentrations were 1.75 and 1.5 μCi/ml, respectively, as these uptake values relative to normal tissues—3:1 and 6:1—have been noted clinically.[19]

We used NCAT software to generate a CT-like image of linear attenuation coefficients for 140 keV photons in the following tissues: 0.149–0.157 cm^{-1} in soft tissues and 0.163–0.220 cm^{-1} in bone. The attenuation phantom had the exact geometry of the activity phantom. The couch was assigned a linear coefficient of 0.250 cm^{-1}, which corresponds to a predominately carbon-based material with physical density of 1.8 g/cm^3.[21] A map of attenuation coefficients and dimensions for a slice containing tumor are shown in Fig. 2.

The effects of respiration were considered by averaging 16 phases of a respiratory cycle where the diaphragm moved 20.0 mm and the chest expanded by 12.0 mm. Normal structures experienced varying degrees of 2D motion in the anteroposterior (AP) and superoinferior (SI) dimensions. Identical motion vectors were applied to laterally symmetric left- and right-sided lung tumors to minimize differences other than activity concentration. Lung tumor motion was characterized by one of four maximum centroid-to-centroid displacements according to tumor location: anteromedial (7.20 mm SI, 7.20 mm AP), anterolateral (10.8 mm SI, 10.8 mm AP), posteromedial (7.20 mm SI, 3.60 mm AP), posterolateral (10.8 mm SI, 3.60 mm AP). Tumors outside the lungs were stationary. Activity and attenuation phantoms were implemented on a $384\times384\times384$ grid of 0.18-cm-wide voxels. Attenuation phantoms, one for each tumor size, were also placed on a coarser grid with 0.36-cm-wide voxels and were used to correct for nonuniform attenuation during reconstruction.

II.B. Projection data simulation and image reconstruction

SPECT imaging was simulated with an analytical, ray-driven software using the code SPECT-MAP which has been utilized and tested in this and many previous studies, e.g., Refs. 22–26. Projection images were modeled for a gamma camera with 46×23 cm^2 active surface area and parallel-hole, low-energy, high-resolution collimation. Simulated collimator holes were 2.7 cm long by 0.14 cm in diameter.

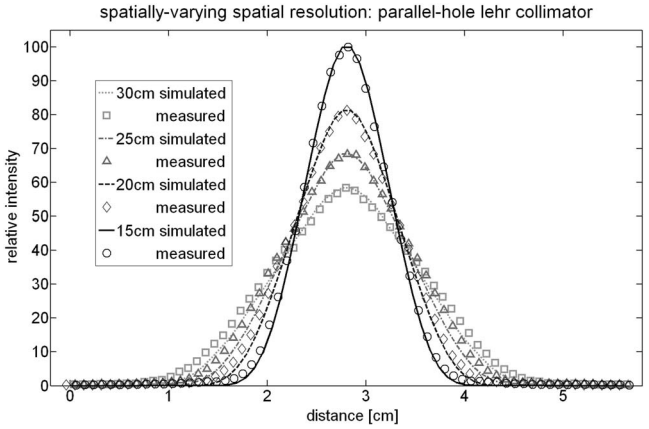

FIG. 3. Line source profiles for measured and simulated data that show the effects of distance-dependent collimator resolution. Measurements were made with a Trionix Triad SPECT scanner.

Distance-dependent spatial resolution was determined by fitting an analytical form to measured projection data. This spatial resolution modeling was implemented by tracing a cone of 121 rays from multiple subdivisions of each detector bin. The resolution modeling was validated by comparing measured line spread functions to those calculated using 121-ray cones, as shown in Fig. 3. Intrinsic resolution was modeled with a 2D, 0.34-cm-FWHM Gaussian kernel. Also modeled were the efficiencies of the collimator, scintillator, and branching ratio of ^{99m}Tc. SPECT-MAP calculations of efficiency and attenuation were checked against hand calculations. Scatter was not considered.

Projection images were simulated for step-and-shoot mode every 3° over a half-circular trajectory by rotating the detector from right lateral over the chest to left lateral as shown in Fig. 4. Bins in projection images were 0.36 cm wide. Finite bin width was modeled by tracing four cones from each bin, i.e., one cone from the center of the four quadrants; thus in total $4\times121=484$ rays were traced from each detector bin. The detector-to-image-plane radius of rotation was 26.5 cm with the axis of rotation centered near the phantom spine. Using this detector and trajectory, there was no truncation of the transaxial slices containing tumors, as demonstrated in Fig. 4 by the dashed line that encloses the common volume, i.e., the region that is projected onto the detector surface at every angle. These simulated noise-free 2D projection images were degraded with varying levels of Poisson noise corresponding to scan times of 4, 8, and 20 min. Ensembles of 25 independent noisy projection images were generated for each combination of scan time and tumor size.

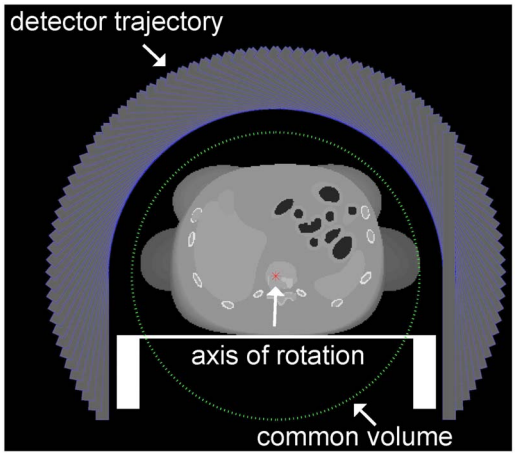

FIG. 4. Detector trajectory spanning 180° anteriorly is displayed with overlapping gray bars. Axis of rotation is marked with an asterisk. Common volume—voxels projected onto the detector at every view—is inside the dashed line.

Image ensembles were reconstructed via ordered-subsets expectation maximization (OSEM) (Ref. 27) using six subsets and five iterations, which are in the range of typically used values.[28] Attenuation correction was achieved by modeling photon detection probabilities within OSEM. In the reconstructed images, the intensities of deep background regions were similar to those in the phantom, thus validating attenuation correction. Our reconstructions did not model distance-dependent spatial resolution, as is typical of most clinical SPECT imaging. Image voxels were 0.36 cm wide, a factor of 2 coarser than voxels of grids on which phantoms were placed for simulating projections. During reconstruction, four rays were traced from every projection bin through the reconstruction grid in order to average over the finite detector bin width. Rays were oriented perpendicular to the image plane and spaced equally from one another in the transaxial dimension of a bin. Additional rays were not traced along the axial (superior-inferior) dimension because of the exact axial alignment between projection bins and image voxels at every detector view. Noisy reconstructed images were smoothed with 3D Gaussian kernels of 8, 14, and 20 mm FWHMs.

II.C. Image analysis

Contrast-to-noise ratios (CNRs) and localization metrics were calculated from noisy image ensembles. For CNR calculations, 3D ROIs were drawn around the tumor. Approximately 7.2 mm away from these ROI boundaries, shell-like ROIs were defined in the background. ROIs were approximately spherical for stationary tumors. For lung tumors, ROIs were irregularly shaped so as to account for the asymmetric blurring effects of respiratory motion. Both tumor and background ROIs were the size of tumor volumes and encompassed 21, 45, and 139 voxels for respective tumor diameters of 10.8, 14.4, and 21.6 mm.

Contrast was defined as

$$C_i = \frac{\overline{T_i} - \overline{B_i}}{\overline{B_i}}, \tag{1}$$

where $\overline{T_i}$ and $\overline{B_i}$ are mean tumor and background ROI intensities in image i. Mean contrast,

$$\hat{C} = \frac{\sum_{i=1}^{N} C_i}{N}, \tag{2}$$

was calculated from the $N=25$ noisy reconstructed images. This definition of contrast allows for negative values when the background is hotter than the tumor in order to avoid upward bias of mean contrast values when background noise dominates the tumor signal. Noise was calculated as the standard deviation of contrast:

$$\sigma_{\hat{C}} = \sqrt{\frac{\sum_{i=1}^{N}(C_i - \hat{C})^2}{N-1}}. \tag{3}$$

Ensemble average contrast-to-noise ratio was

$$\mathrm{CNR} = \frac{\hat{C}}{\sigma_{\hat{C}}}. \tag{4}$$

Localization accuracy and precision were assessed by calculating the mean and standard deviation of distances between true and measured tumor centroids over ensembles of noisy reconstructed images. Tumor locations in noisy images were selected via a forced choice task using nonprewhitening filters.[29–31] This approach is relevant to radiation therapy delivery because disease is known to exist; yet the exact position varies with each time the patient is positioned on the treatment table.

Since the approximate tumor location is known from treatment-planning images, the search can be limited to a relatively small volume. In this study, 3D search volumes—14.4-mm-radius spherical ROIs—were defined around each tumor. The size of each search volume was intended to encompass the uncertainties in tumor location that are typical for radiation therapy. Each search volume contained 257 voxels that were subdivided three times in each dimension. The location in the ROI that had the highest cross correlation (XC) with a noise-free tumor template was selected as the measured tumor centroid:

$$\mathrm{XC}_i = \frac{\mathrm{template}_j \cdot \mathrm{image}_i}{\sqrt{(\mathrm{template}_j \cdot \mathrm{template}_j)(\mathrm{image}_i \cdot \mathrm{image}_i)}}, \tag{5}$$

$$r_{m,i} = \arg\max_{j \in \Omega}(\mathrm{XC}_{i,j}), \tag{6}$$

where $\mathrm{template}_j$ represents the template centered at voxel j within ROI Ω of ensemble image i. The denominator in the above cross-correlation equation normalizes the response such that it does not depend on voxel intensities. As such cross-correlation values were suppressed for hot background structures (e.g., heart) that would have otherwise elicited greater responses than the nearby tumor. Tumor templates were generated by convolving true tumor geometries with a 14.4-mm-Gaussian kernel that approximates typical spatial resolutions in these images. For lung tumors, the true tumor geometry included asymmetric blurring from respiratory motion. Tumor templates were constructed on cubic grids of 0.12-cm-wide voxels with grid widths of 27, 33, and 39 voxels for tumor diameters of 10.8, 14.4, and 21.6 mm, respectively.

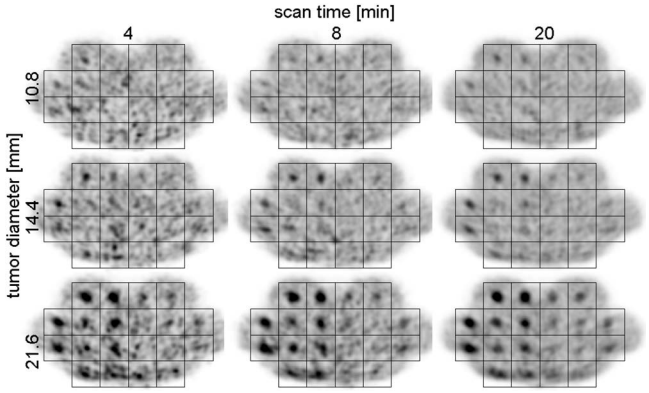

FIG. 5. Sample reconstructed images, smoothed with 14-mm-FWHM Gaussian, for each combination of tumor size and scan time.

Mean localization error $\overline{dr}$ was defined as the offset distance dr between true $r_t=(x_t,y_t,z_t)$ and measured tumor centroids $r_{m,i}=(x_{m,i},y_{m,i},z_{m,i})$ averaged over the ensemble of $N=25$ noisy reconstructed images:

$$dr = \sqrt{(x_m - x_t)^2 + (y_m - y_t)^2 + (z_m - z_t)^2}, \tag{7}$$

$$\overline{dr} = \frac{1}{N}\sum_{i=1}^{N} dr_i. \tag{8}$$

Standard deviation in localization error was computed as

$$\sigma_{dr} = \sqrt{\frac{\sum_{i=1}^{N}(dr_i - \overline{dr})^2}{N-1}}. \tag{9}$$

III. RESULTS

III.A. Reconstructed images

Reconstructed images for each combination of tumor diameter and scan time are presented in Fig. 5. These images are noisy realizations, not ensemble averages, and have been smoothed with a 3D, 14-mm-FWHM Gaussian kernel. Grids are superimposed on images such that each square element is centered on a tumor.

Qualitative trends are apparent in these images. As scan time increases, noise decreases, thereby improving the tumor visibility. For instance, with the 4 min scans, image noise resembles the expected signal for 10.8 and 14.4 mm diameter tumors in some locations, especially in the lungs and near posterior of the phantom. When scan time is increased to 8 and then 20 min, there are fewer and fewer hot spots off center of the grid, which suggests that the apparent activity is the true tumor signal. Tumor-to-background uptake ratios have a substantial effect on tumor visibility, as those on the patient right side with 6:1 uptake ratios are more noticeable than left-sided tumors with 3:1 uptake ratios. Also note the impact of tumor location relative to the detector trajectory: Tumors near the chest wall, which are on average closer to the detector, are strikingly more apparent than lung tumors and stationary tumors near the spine. The detector trajectory also affects apparent tumor shape. Anterior tumors are ap-

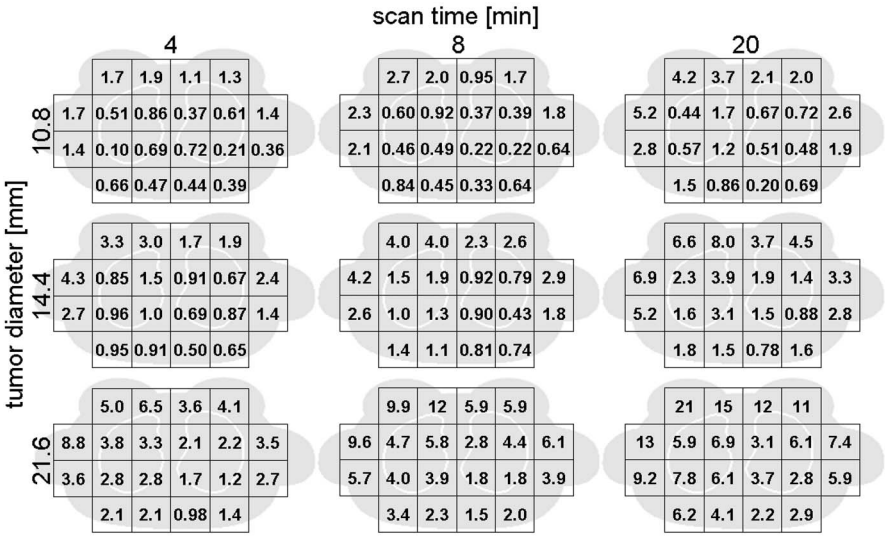

FIG. 6. CNRs calculated from ensembles of noisy reconstructed images and presented as a function of location for each combination of scan time and tumor diameter.

proximately circular, while other visible tumors are elliptical with varying degrees of eccentricity. Greater eccentricity occurs when the detector-to-tumor distance is substantially different over the detector trajectory.

III.B. Contrast-to-noise ratio

CNRs were calculated from ensembles of noisy reconstructed images using Eqs. (1)–(4). CNR values are displayed in Fig. 6 as a function of anatomy for the investigated scan times and tumor diameters. Many of the visual trends noted in the reconstructed images from Fig. 5 are expressed quantitatively in Fig. 6 as ensemble CNRs. CNRs increase approximately by the square root of imaging time. Right-sided tumors with 6:1 radiotracer uptake ratios have higher CNRs than their laterally symmetric counterparts of 3:1 uptake by an average factor of 1.6. CNRs of anterior tumors are typically 3.5 times greater than their posterior counterparts. These trends are shown in Fig. 7, thus demonstrating the relative impact of radiotracer uptake versus the detector trajectory on CNR.

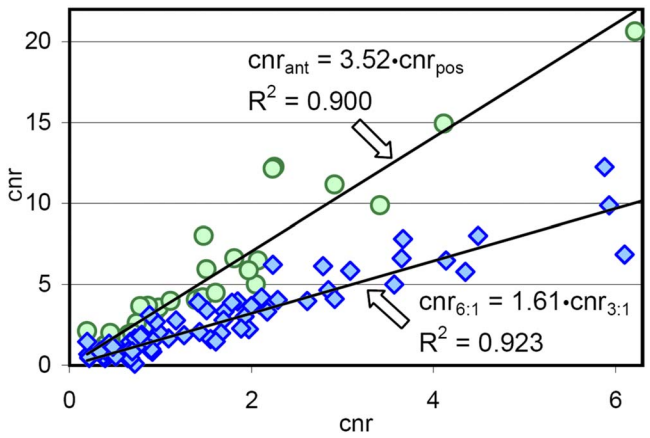

FIG. 7. Differences in CNR due to radiotracer uptake and anatomical location. Circles represent differences in CNR between anterior tumors and their posterior counterparts. Diamonds indicate the CNRs of laterally symmetric tumors that differ by radiotracer uptake.

III.C. Localization

Localization metrics—the mean localization error $\overline{dr}$ and ensemble standard deviation σ_{dr}—were calculated using Eqs. (5)–(9) and are reported in Fig. 8. Mean errors are represented by white and black boxes that respectively correspond to tumors of 6:1 and 3:1 radiotracer uptakes. Error bars indicate standard deviations. The different tumor sizes are separated by rows. Columns differentiate tumor locations. Note the diagram above each column in Fig. 8 that specifies anatomical locations. Within each column there are six data points—three white and three black boxes—that correspond to scan times of 4, 8, and 20 min for each uptake ratio. When viewing Fig. 8 from left to right, tumor locations vary from anterior to lateral to posterior. A bold dashed line separates stationary and lung tumors. The relative order of lung tumors is the same as that of stationary tumors.

In all but the regions of poorest SPECT image quality, tumors of 6:1 uptake are typically localized as accurately with 4 min of scan time as tumors of 3:1 uptake that are imaged for 20 min. This trend is demonstrated in Fig. 8 by observing the relative height of boxes, specifically the first white and the third black boxes within a column. For locations at which noise and blur are severe, localization is determined primarily by random chance for both 3:1 and 6:1 uptake ratios. In these cases, localization accuracy is similar and poor for the two uptake ratios. This effect is illustrated by the 10.8 mm tumors in the lungs.

Tumor location has a major impact on localization accuracy. In Fig. 8, there is a general trend where localization errors worsen when tumor location changes from anterior to lateral to posterior. As with CNRs, tumor location relative to the detector trajectory can have a larger effect on localization error than radiotracer uptake ratio. These effects are shown in Fig. 8 when making comparisons among stationary tumors near the chest wall of different uptake ratios, and then with

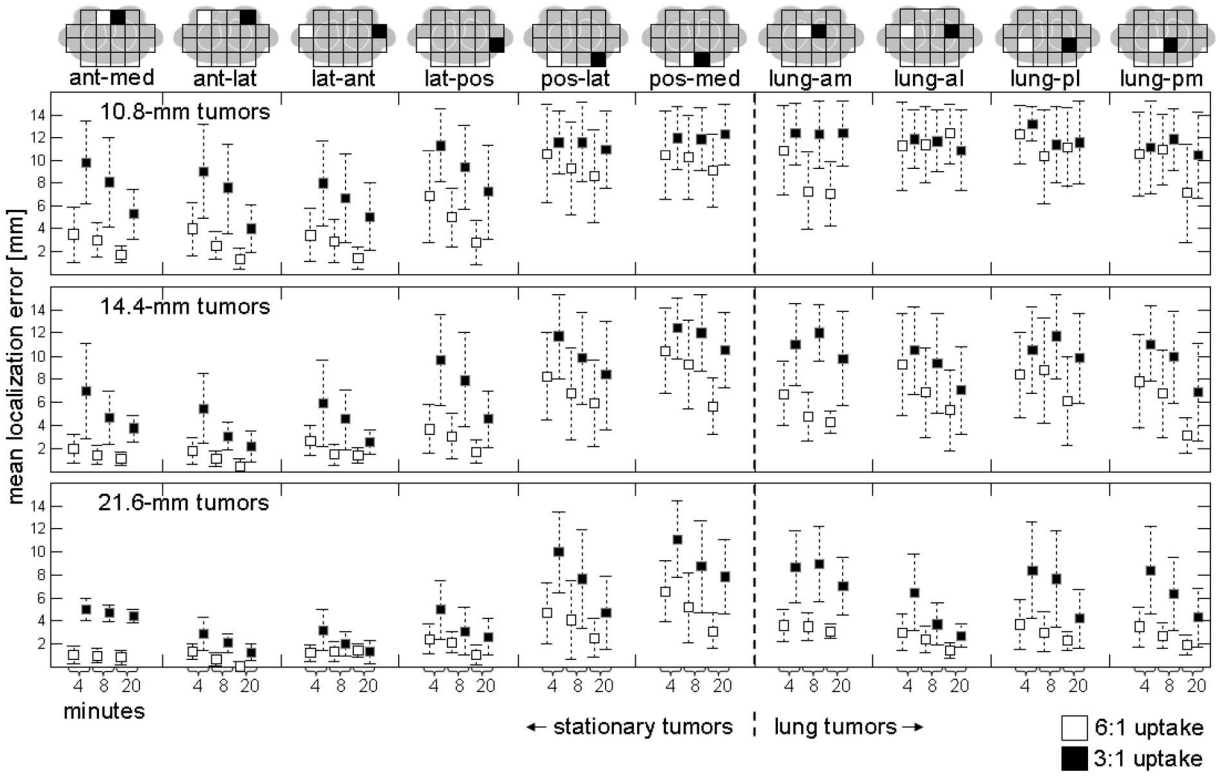

FIG. 8. Ensemble localization errors for different combinations of tumor size, location, radiotracer uptake, and imaging time. Mean errors are displayed as black and white boxes for respective uptake ratios of 3:1 and 6:1. Error bars indicate standard deviations. Tumor sizes are separated by rows and tumor locations by columns. Within each column, there are six data points that correspond with scan times of 4, 8, and 20 min for laterally symmetric tumors of different uptake ratios.

counterparts near the spine and posterior ribs. Though localization is generally poor for posterior tumors, certain results are encouraging. When using relatively short 4 min scans, anterior tumors with diameters of 14.4 and 21.6 mm and 6:1 uptake ratios had mean localization errors less than 2 mm.

III.D. Localization accuracy as a function of contrast-to-noise ratio

Mean localization errors are plotted as a function of CNRs in Fig. 9. There is a noticeable trend. When CNRs are close to zero, localization errors are around 11 mm, which is the expected error when randomly selecting radial locations from a 14.4-mm-radius search volume. In this regime, noise dominates and SPECT provides very little information. As CNRs increase to around 5, localization errors improve rapidly because SPECT is providing more information. Improvements in localization are more modest as CNRs continue to increase. In this region, there is comparatively less to gain from enhancing the already pronounced tumor signal.

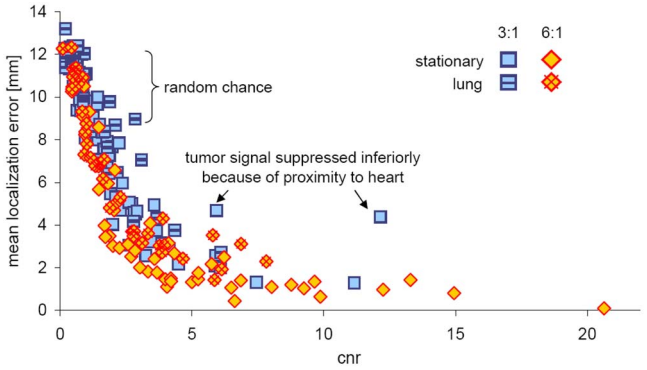

FIG. 9. Mean localization errors plotted as a function of CNRs. Tumors of 3:1 and 6:1 uptakes are differentiated by square and diamond markers. Markers that are crossed signify lung tumors, while solid markers represent stationary tumors.

There are other more subtle effects in Fig. 9. In the CNR range of 3–5, localization is typically better for tumors of 6:1 than 3:1 uptake. Localization error is generally better for stationary tumor of the same uptake ratio than lung tumors with similar CNRs. Two stationary tumors of 3:1 uptake with relatively high CNRs are noticeably skewed above the other data points. The unexpected degradation in localization error is attributable to proximity to the heart where radiotracer concentrations are much higher and suppress tumor signal inferiorly. These results show potential challenges for localizing targets near a hot background.

IV. DISCUSSION

In this simulation study, on-board SPECT was investigated for localizing functional and molecular targets. Several parameters were considered: Scan time and tumor location, diameter, and uptake ratio. Among these, one of the most influential factors was radiotracer uptake in tumor relative to

background: As indicated by CNRs, localization metrics, and visual inspection. Tumors of 6:1 uptake were strikingly more noticeable than their laterally symmetric counterparts of 3:1 uptake. These visual observations were supported by quantitative values—CNRs and localization accuracy. CNRs were on average 1.6 times greater for the tumors of 6:1 radiotracer specificity. The observed ratio of 1.6 is less than the true phantom contrast ratio of 2.5. In the absence of spatial resolution modeling, blurring from limited spatial resolution has a relatively greater impact on contrast recovery of 6:1 tumors compared with those of 3:1 uptake. This result is consistent with the findings of Ref. 32 where scatter, a type of blurring, more substantially reduced the recovered contrast of hotter lesions.

Typically, tumors of 6:1 uptake were localized as accurately using 4 min scans as 3:1 tumors that had been imaged for 20 min. This difference in time has important implications, especially in the context of radiation therapy delivery where short scans are important in minimizing patient motion and ensuring machine throughput. Thus, radiotracer specificity will be an important criterion when selecting or developing potential radiotracers for on-board SPECT imaging. Conversely, diagnostic or treatment-planning SPECT images could be used to estimate tumor characteristics—radiotracer uptake and size—that affect localization in a predictable way in order to gauge whether individual patients would benefit from on-board SPECT. Further, diagnostic or treatment-planning SPECT images could provide radiotracer-concentration templates for estimating localization. Such templates may be particularly useful for localizing tumors with inhomogeneous radiotracer uptake that is comparable in width to, or wider than, the on-board SPECT spatial resolution.

This study utilized a 180° orbit in order to avoid viewing the patient through the couch. Radiation therapy couches are thicker and wider than typical diagnostic imaging couches, such that SPECT data acquired through the couch would be substantially attenuated, and the SPECT detector would be displaced away from the patient, thereby degrading spatial resolution. Averaging over all angles of the 180° orbit, tumors near the chest wall are on average closer to the detector, which implies better spatial resolution, and they are less attenuated by tissue. Because of attenuation, image noise was greater near the spine than the chest wall. Quantum noise is not reversible even with attenuation correction. As is typical for most clinical SPECT imaging, the reconstructions did not model spatial resolution. Consequently, poorer spatial resolution and poorer contrast are expected for the posterior tumors. Modeling spatial resolution would increase image reconstruction time—an important consideration for on-board SPECT. That noted, spatial resolution modeling is worth evaluating in a future study, since it has potential to improve localization.[33] Because localization is better in regions proximal to the detector trajectory and since tumor location is known approximately, on-board SPECT trajectories could be optimized for imaging specific tumor sites.

CNR and localization error are related, but one metric may not necessarily be a good predictor of the other. In this study, noisy reconstructed images were smoothed using Gaussian kernels with FWHMs of 8, 14, and 20 mm. CNRs and localization errors were calculated for noisy images and for images with each degree of smoothing. CNRs improved with smoothing. In contrast, localization errors improved at certain anatomical locations but worsened for others. On average localization errors were comparable across different degrees of smoothing. These results demonstrate that localization errors cannot be estimated directly from CNRs. Encouragingly, these results also suggest that localization accuracy is somewhat robust to smoothing. It follows that they may be robust to iteration number when using iterative reconstruction since smoothness is highly correlated with iteration number. Smoothing did, however, impact localization for certain tumors, and these effects need to be studied further.

CT provides anatomical information that would be valuable for correcting nonuniform attenuation in on-board SPECT images. Attenuation coefficients could be estimated from on-board cone beam CT or from registered CT images.

We do not anticipate that on-board SPECT imaging would be used for every fraction in a highly fractionated treatment because of associated imaging time and patient dose. On-board SPECT is better suited for treatments with a limited number of fractions such as stereotactic body radiation therapy (SBRT). SBRT is used to treat a variety of tumors, including breast oligometastasis.[34,35] For SBRT, imaging time is less of an issue because additional time is allotted for patient positioning as compared with most highly fractioned treatments. Concerning patient dose, a typical 25 mCi injection of ^{99m}Tc-sestamibi[36] results in an effective dose of 7.9 mSv,[37] which is about 1/3 the effective dose of an on-board CBCT chest scan.[38] Cost is also an issue that would have to be evaluated along with any improvements in morbidity and/or mortality through clinical studies.

Localization values may change depending on the coarseness of image voxels or the size of the search volume. In this study, centroids were estimated on a voxelized grid, limited by the half width of a subvoxel. Localization would likely worsen by using a larger search volume with more locations where random noise fluctuations could mimic tumor, particularly for barely visible tumors.

Our simulation study makes absolute estimates regarding localization. Localization values will change—likely for the worse as additional factors such as scatter (estimated to account for 20%–40% of the detected counts in scanner data[39]), tumor diffuseness, and tumor inhomogeneities are considered. Localization accuracy, however, will likely change for the better as trajectories are focused on the target region, as scatter correction is implemented, and as estimation methods are developed specifically for tumor inhomogeneities. This current study contributes as a significant first step, by incorporating a significant degree of realism (e.g., spatial resolution and attenuation), clearly defining that level of realism, and then returning absolute numbers for localization accuracy and precision. Such absolute estimates are necessary in order to access whether on-board SPECT is even

possibly feasible, and these estimates form a baseline which will help in quantifying and understanding the effects of future developments.

V. CONCLUSION

SPECT imaging was investigated for localizing functional and molecular targets immediately prior to radiation therapy. CNRs and localization errors were analyzed as a function of scan time and tumor size, location, and radiotracer uptake using computer simulations. Localization errors were less than 2 mm for certain tumors using relatively short 4 min scans. These encouraging results warrant further investigation of on-board SPECT for localizing functional and molecular targets.

ACKNOWLEDGMENTS

This project was supported in part by NIH Grant No. T32EB007185 from the National Institute of Biomedical Imaging and Bioengineering and by the Department of Defense Breast Cancer Research Program Predoctoral Fellowship (Grant No. BC073559). The content is solely the responsibility of the authors and does not necessarily represent the official views of the National Institute of Biomedical Imaging and Bioengineering, the National Institutes of Health, or the Department of Defense. The authors would like to thank the reviewers for helpful comments which have improved the paper.

[a]Author to whom correspondence should addressed. Electronic mail: justin.roper@duke.edu; Tel.: (919)-688-0489; Fax: (919)-681-7183.

[1]J. D. Chapman, J. D. Bradley, J. F. Eary, R. Haubner, S. M. Larson, J. M. Michalski, P. G. Okunieff, H. W. Strauss, Y. C. Ung, and M. J. Welch, "Molecular (functional) imaging for radiotherapy applications: An RTOG symposium," Int. J. Radiat. Oncol., Biol., Phys. **55**, 294–301 (2003).

[2]C. C. Ling, J. Humm, S. Larson, H. Amols, Z. Fuks, S. Leibel, and J. A. Koutcher, "Towards multidimensional radiotherapy (MD-CRT): Biological imaging and biological conformality," Int. J. Radiat. Oncol., Biol., Phys. **47**, 551–560 (2000).

[3]L. A. Dawson and D. A. Jaffray, "Advances in image-guided radiation therapy," J. Clin. Oncol. **25**, 938–946 (2007).

[4]L. A. Dawson, K. K. Brock, S. Kazanjian, D. Fitch, C. J. McGinn, T. S. Lawrence, R. K. Ten Haken, and J. Balter, "The reproducibility of organ position using active breathing control (ABC) during liver radiotherapy," Int. J. Radiat. Oncol., Biol., Phys. **51**, 1410–1420 (2001).

[5]M. Guckenberger, J. Meyer, J. Wilbert, K. Baier, G. Mueller, J. Wulf, and M. Flentje, "Cone-beam CT based image-guidance for extracranial stereotactic radiotherapy of intrapulmonary tumors," Acta Oncol. **45**, 897–906 (2006).

[6]J. M. Schallenkamp, M. G. Herman, J. J. Kruse, and T. M. Pisansky, "Prostate position relative to pelvic bony anatomy based on intraprostatic gold markers and electronic portal imaging," Int. J. Radiat. Oncol., Biol., Phys. **63**, 800–811 (2005).

[7]S. A. Nehmeh, N. Y. Lee, H. Schroder, O. Squire, P. B. Zanzonico, Y. E. Erdi, C. Greco, G. Mageras, H. S. Pham, S. M. Larson, C. C. Ling, and J. L. Humm, "Reproducibility of intratumor distribution of (18)F-fluoromisonidazole in head and neck cancer," Int. J. Radiat. Oncol, Biol., Phys. **70**, 235–242 (2008).

[8]Z. Keidar, O. Israel, and Y. Krausz, "SPECT/CT in tumor imaging: Technical aspects and clinical applications," Semin. Nucl. Med. **33**, 205–218 (2003).

[9]C. Zhu, "Eighth Asia and Oceania Congress of Nuclear Medicine and Biology," October 9–13, 2004, Beijing, China. J. Nucl. Med. **45**, 13N–16N (2004).

[10]D. J. Yang, E. E. Kim, and T. Inoue, "Targeted molecular imaging in oncology," Ann. Nucl. Med. **20**, 1–11 (2006).

[11]K. T. Cheng, A. Menkens, S. Bryant, and D. C. Sullivan, "NIH MICAD initiative and guest author program opportunities," J. Nucl. Med. **48**, 19N (2007).

[12]M. Hamoudeh, M. A. Kamleh, R. Diab, and H. Fessi, "Radionuclides delivery systems for nuclear imaging and radiotherapy of cancer," Adv. Drug Delivery Rev. **60**, 1329–1346 (2008).

[13]S. K. Imam, "Molecular nuclear imaging: The radiopharmaceuticals," Cancer Biother. Radiopharm. **20**, 163–672 (2005).

[14]R. Schibli and P. A. Schubiger, "Current use and future potential of organometallic radiopharmaceuticals," Eur. J. Nucl. Med. Mol. Imaging **29**, 1529–1542 (2002).

[15]Q. F. Xiong and Y. Chen, "Review: Deoxyglucose compounds labeled with isotopes different from 18-fuoride: Is there a future in clinical practice?," Cancer Biother. Radiopharm. **23**, 376–381 (2008).

[16]W. P. Segars and B. M. Tsui, "Study of the efficacy of respiratory gating in myocardial SPECT using the new 4D NCAT Phantom," IEEE Trans. Nucl. Sci. **49**, 675–679 (2002).

[17]B. M. W. Tsui, W. P. Segars, and D. S. Lalush, "Effects of upward creep and respiratory motion in myocardial SPECT," IEEE Transactions on Nuclear Science **47**(3), 1192–1195 (2000).

[18]A. Spanu, O. Schillaci, and G. Madeddu, "Tc-99m labelled cationic lipophilic complexes in malignant and benign tumors: The role of SPET and pinhole-SPET in breast cancer, differentiated thyroid carcinoma and hyperparathyroidism," Q. J. Nucl. Med. Mol. Imaging **49**, 145–169 (2005).

[19]J. Maublant, M. deLatour, D. Mestas, A. Clemenson, S. Charrier, V. Feillel, G. Le Bouedec, P. Kaufmann, J. Dauplat, and A. Veyre, "Technetium-99m-sestamibi uptake in breast tumor and associated lymph nodes," J. Nucl. Med. **37**, 922–925 (1996).

[20]A. Chiti, L. S. Maffioli, M. Infante, G. Grasselli, M. Incarbone, M. D. Gasparini, G. Savelli, and E. Bombardieri, "Assessment of mediastinal involvement in lung cancer with technetium-99m-sestamibi SPECT," J. Nucl. Med. **37**, 938–942 (1996).

[21]B. Poppe, N. Chofor, A. Ruhmann, W. Kunth, A. Djouguela, R. Kollhoff, and K. C. Willborn, "The effect of a carbon-fiber couch on the depth-dose curves and transmission properties for megavoltage photon beams," Strahlenther. Onkol. **183**, 43–48 (2007).

[22]J. E. Bowsher, D. M. DeLong, T. G. Turkington, and R. J. Jaszczak, "Aligning emission-tomography and MRI images by optimizing the emission-tomography image reconstruction objective function," IEEE Trans. Nucl. Sci. **53**, 1248–1258 (2006).

[23]J. E. Bowsher, M. P. Tornai, J. Peter, D. E. Gonzalez Trotter, A. Krol, D. R. Gilland, and R. J. Jaszczak, "Modeling the axial extension of a transmission line source within iterative reconstruction via multiple transmission sources," IEEE Trans. Med. Imaging **21**, 200–215 (2002).

[24]D. E. G. Trotter, J. Bowsher, and R. Jaszczak, "Absolute quantitation of a spherical I-131 activity distributions using a high-resolution rotating collimator: A phantom study," IEEE Trans. Nucl. Sci. **48**, 65–73 (2001).

[25]C. N. Archer, M. P. Tornai, J. E. Bowsher, S. D. Metzler, B. C. Pieper, and R. J. Jaszczak, "Implementation and initial characterization of acquisition orbits with a dedicated emission mammotomograph," IEEE Trans. Nucl. Sci. **50**, 413–420 (2003).

[26]R. Ter-Antonyan, R. J. Jaszczak, J. E. Bowsher, K. L. Greer, and S. D. Metzler, "Brain SPECT simulation using half-cone-beam collimation and single-revolution helical-path acquisition," IEEE Transactions on Nuclear Science **54**, 475–479 (2007).

[27]H. M. Hudson, B. F. Hutton, and P. Larkin, "Accelerated EM reconstruction using ordered subsets," J. Nucl. Med. **33**, 960 (1992).

[28]A. Seret, "The number of subsets required for OSEM reconstruction in nuclear cardiology," Eur. J. Nucl. Med. Mol. Imaging **33**, 231 (2006).

[29]H. C. Gifford, P. E. Kinahan, C. Lartizien, and M. A. King, "Evaluation of multiclass model observers in PET LROC studies," IEEE Trans. Nucl. Sci. **54**, 116–123 (2007).

[30]H. C. Gifford, M. A. King, P. H. Pretorius, and R. G. Wells, "A comparison of human and model observers in multislice LROC studies," IEEE Trans. Med. Imaging **24**, 160–169 (2005).

[31]C. Lartizien, P. E. Kinahan, and C. Comtat, "Volumetric model and human observer comparisons of tumor detection for whole-body positron emission tomography," Acad. Radiol. **11**, 637–648 (2004).

[32]J. E. Bowsher and C. E. J. Floyd, "Treatment of Compton scattering in maximum-likelihood, expectation-maximization reconstructions of SPECT images," J. Nucl. Med. **32**, 1285–1291 (1991).

[33]H. C. Gifford, M. A. King, R. G. Wells, W. G. Hawkins, M. V. Narayanan, and P. H. Pretorius, "LROC analysis of detector-response compen-

sation in SPECT," IEEE Trans. Med. Imaging **19**, 463–473 (2000).
[34]H. Blomgren, I. Lax, I. Naslund, and R. Svanstrom, "Stereotactic high dose fraction radiation therapy of extracranial tumors using an accelerator. Clinical experience of the first thirty-one patients," Acta Oncol. **34**, 861–870 (1995).
[35]M. T. Milano, A. W. Katz, M. C. Schell, A. Philip, and P. Okunieff, "Descriptive analysis of oligometastatic lesions treated with curative-intent stereotactic body radiotherapy," Int. J. Radiat. Oncol., Biol., Phys. **72**, 1516–1522 (2008).
[36]I. Khalkhali, J. Villanueva-Meyer, S. L. Edell, J. L. Connolly, S. J. Schnitt, J. K. Baum, M. J. Houlihan, R. M. Jenkins, and S. B. Haber, "Diagnostic accuracy of 99mTc-sestamibi breast imaging: multicenter trial results," J. Nucl. Med. **41**, 1973–1979 (2000).
[37]Radiological Protection in Biomedical Research, "A report of Committee 3 adopted by the International Commission on Radiological Protection," Ann. ICRP **22**, 1–28 (1991).
[38]M. W. Kan, L. H. Leung, W. Wong, and N. Lam, "Radiation dose from cone beam computed tomography for image-guided radiation therapy," Int. J. Radiat. Oncol., Biol., Phys. **70**, 272–279 (2008).
[39]Y. S. Gur, T. H. Farncombe, P. H. Pretorius, H. C. Gifford, M. V. Narayanan, E. C. Frey, D. Gagnon, and M. A. King, *Comparison of Scatter Compensation Strategies for Cardiac Perfusion Imaging using Tc-99m labeled sestamibi Nuclear Science Symposium Conference Record*, 2001 (IEEE, 2001), pp. 2188–2192.